Journal of Geophysical Research: Space Physics

RESEARCH ARTICLE
10.1029/2018JA025669

Quiet Daytime Arctic Ionospheric *D* Region

Neil R. Thomson[1], **Mark A. Clilverd**[2], **and Craig J. Rodger**[1]

[1]Physics Department, University of Otago, Dunedin, New Zealand, [2]British Antarctic Survey, Cambridge, UK

Key Points:
- Daytime Arctic ionospheric *D* region height and sharpness measured as 73.7 km and 0.32 km^{-1} using long VLF radio path Germany to Alaska
- Daytime Arctic *D* region largely independent of solar zenith angle unlike at lower latitudes where solar Lyman alpha dominates
- Energetic particle precipitation is just dominant over galactic cosmic rays and solar Lyman alpha in the quiet daytime Arctic *D* region

Supporting Information:
- Supporting Information S1
- Data Set S1

Correspondence to:
N. R. Thomson,
thomsoneil@gmail.com

Citation:
Thomson, N. R., Clilverd, M. A., & Rodger, C. J. (2018). Quiet daytime Arctic ionospheric *D* region. *Journal of Geophysical Research: Space Physics*, *123*, 9726–9742. https://doi.org/10.1029/2018JA025669

Received 11 MAY 2018
Accepted 20 OCT 2018
Accepted article online 26 OCT 2018
Published online 9 NOV 2018

©2018. American Geophysical Union. All Rights Reserved.

Abstract Phase and amplitude measurements of VLF radio waves propagating subionospherically on long paths across the Arctic are used to determine the high latitude, daytime *D* region height, and sharpness of the bottom edge of the Earth's ionosphere. The principal path used is from the 23.4-kHz transmitter, DHO, in north Germany, northward across the Arctic passing ~2° from the North Pole, and then southward to Nome, Alaska, thus avoiding most land and all thick ice. Significant observational support is obtained from the also nearly all-sea path from JXN in Norway (~67°N, 16.4 kHz) across the North Pole to Nome. By suitably comparing measurements with modeling using the U.S. Navy code LWPC, the daytime *D* region (Wait) height and sharpness parameters in the Arctic are found to be $H' = 73.7 \pm 0.7$ km and $\beta = 0.32 \pm 0.02$ km^{-1} in the summer of 2013, that is, at (weak) solar maximum. It is also found that, unlike at lower latitudes, very low frequency phase and amplitude recordings on (~1,000 km) paths at high subarctic latitudes show very little change with solar zenith angle in both phase and amplitude during daytime for solar zenith angles <~80°. It is concluded that, at high latitudes, the daytime lower *D* region is dominated by nonsolar ionizing sources in particular by energetic particle precipitation (>~300 keV for electrons) with a contribution from galactic cosmic rays, rather than by solar Lyman α which dominates at low and middle latitudes.

1. Introduction

The lower *D* region forms the bottom edge of the Earth's ionosphere; that is, it covers the lowest height range for which there are sufficient free electrons to have significant effects on radio waves, such as attenuation and (partial) reflections. During daytime this height range is typically ~50–80 km with the bulk of the free electrons in the upper part of this range, in low and middle latitudes, being generated by solar Lyman α ionizing the minor neutral constituent NO. In the lower part of this range (omnidirectional) galactic cosmic rays generate the bulk of the free electrons by partially ionizing all the different air molecules (e.g., Banks & Kockarts, 1973; Brasseur & Solomon, 2005).

At low latitudes the geomagnetic field is nearer horizontal and so provides significant shielding from galactic cosmic rays (e.g., Størmer, 1955). At high latitudes the intensity of galactic cosmic rays is ~3–4 times greater than at low latitudes (e.g., Lin et al., 1963), at least at *D* region heights, because the geomagnetic field is nearer vertical and so provides much less shielding. In addition, at low latitudes, in the central part of the day, the (unidirectional) Lyman α from the Sun arrives from near vertical (low solar zenith angle) and penetrates much more deeply into the *D* region than it does at high latitudes where the Sun is far from the vertical (high solar zenith angle). At high latitudes this results in solar Lyman α (which is principally absorbed by O_2) penetrating less deeply in altitude due to the long nearly horizontal distance traveled in the *D* region.

Thus, at low latitudes near midday, solar Lyman α generation of electrons dominates down to below an altitude of 70 km (e.g., Banks & Kockarts, 1973). Away from midday this dominance of Lyman α diminishes toward dawn and dusk because Lyman α electron generation depends on solar zenith angle but galactic cosmic ray electron generation does not. This means that the daylit low-latitude *D* region undergoes significant changes with solar zenith angle (Thomson et al., 2014). In contrast, at middle to high latitudes (~53°), where the Lyman α influence is lower (though still dominant) and the galactic cosmic ray influence is higher, the *D* region has been found to undergo smaller changes with solar zenith angle (Thomson et al., 2017). A key purpose of the high-latitude (Arctic and subarctic) measurements reported in the current study is to determine if electron generation by energetic particle precipitation (EPP) or galactic cosmic rays dominates over solar Lyman α, resulting in minimal changes with solar zenith angle in the daytime *D* region at these high latitudes.

Radio waves with frequencies of ~10–40 kHz, that is, within and just above the very low frequency (VLF) range, have proved very valuable for measuring the lower *D* region (e.g., Thomson et al., 2014, 2017, and references

therein). At these heights satellites experience too much drag to survive long enough to provide useful measurements. Rockets have proved very successful (e.g., Friedrich & Torkar, 2001) but they tend to be too transient and expensive for conveniently determining diurnal, seasonal, latitudinal, and solar cycle variations. Also, VLF radio signals can travel hundreds to many thousands of kilometers by reflecting from the lower *D* region and still allow phase and amplitude measurements at the receiver which are both very stable and rather sensitive to the properties of the *D* region from which they reflect. Ideally the length of the path can be chosen to be long enough to usefully give good averaging over a suitable region but short enough not to average over distinctly different regions (e.g., high/low latitude, midday/dusk/night). These VLF signals reflect not only from the ionospheric *D* region but also from the surface of the ocean or ground below. They are thus often described as traveling in the Earth-ionosphere waveguide or subionospherically (e.g., Watt, 1967).

Ideally VLF paths chosen for determining *D* region parameters should be mainly over the sea because its conductivity is well known and nonvarying. In particular, in the present polar context, thin sea ice, which has typically averaged ~2 m thick, in the vicinity of the North Pole in recent years (e.g., Kwok & Rothrock, 2009; http://www.npolar.no/en/projects/fram-strait-arctic-outflow-observatory.html), has negligible effect on VLF (as discussed later in section 5.2). However, the path should not pass over thick ice (hundreds to thousands of meters thick) such as in Greenland or Antarctica because the effects on the VLF radio propagation would then be major and difficult to allow for with sufficient accuracy. Small amounts of land are accounted for quite well by the U.S. Navy code, longwave propagation capability (LWPC), which includes a worldwide conductivity map (Ferguson & Snyder, 1990; Morgan, 1968). Powerful VLF transmitters are large and expensive so that an existing transmitter was needed for the current study. The transmitter location should also preferably be at a latitude greater than ~50° to avoid having to correct for significant parts of the path not being at high latitudes. Having all the transmitter latitudes in the range 60°–70° would have been ideal, giving long enough paths totally within the region of interest, but this proved too restrictive. A receiver location needs to be reasonably accessible (preferably by a scheduled aircraft flight) approximately on the other side of the North Pole to the transmitter (to get a long path through mainly polar regions) and such that the path does not go over much land or over any thick ice. The very thick ice in the Antarctic is too difficult to model with sufficient accuracy for VLF propagation.

These considerations resulted in the two paths shown in Figure 1 being chosen: (1) the 6,951-km path from the 23.4-kHz transmitter, DHO, in North Germany (53.1°N, 7.6°E) to Nome (64.5°N, 165.4°W), Alaska, which passes within ~230 km of the North Pole and (2) the 5,416-km path from the 16.4-kHz Norwegian transmitter JXN (67.0°N, 13.9°E) to Nome, which passes within ~20 km of the North Pole.

The measurements here are focused on quiet, undisturbed conditions to determine an ionospheric baseline from which perturbations can be measured and interpreted. Such perturbations include those from the various forms of particle precipitation, particularly common in polar regions because of the low geomagnetic shielding (e.g., Neal et al., 2015). Continuous recordings on VLF paths have been made and are continuing to be made by scientific networks such as Antarctic-Arctic Radiation-belt Dynamic Deposition VLF Atmospheric Research Konsortia (AARDDVARK) in order to determine energy inputs into the upper atmosphere from energetic particle precipitation from the observed perturbations (e.g., Clilverd et al., 2009; http://www.physics.otago.ac.nz/space/AARDDVARK_homepage.htm).

Here, again using VLF phase and amplitude measurements, we extend and complete our accurate, all latitude characterizations, of the undisturbed daytime lower *D* region at VLF from near the equator (Thomson et al., 2014) through midlatitudes (Thomson et al., 2017) to the polar regions by now presenting results for the high-latitude Arctic and subarctic regions.

In section 2, we describe the phase and amplitude measurements on our principal polar VLF path, DHO-Nome, and compare these with calculations for a range of appropriate lower *D* region parameters. As discussed in section 2.4, this comparison raises the possibility of an ambiguity of modulo 90° in phase which is resolved in the following sections. In section 3 we use VLF observations to show that high-latitude daytime *D* region parameters are generally much less sensitive to solar zenith angle (SZA) than at lower latitudes. This not only helps to resolve the 90° ambiguity but also avoids the need for SZA corrections along our all-daylight polar paths. In section 4, we analyze our JXN-Nome path which is found to support our analysis of our DHO-Nome results. In section 5, we first make a small adjustment for the DHO-Nome results allowing for the small

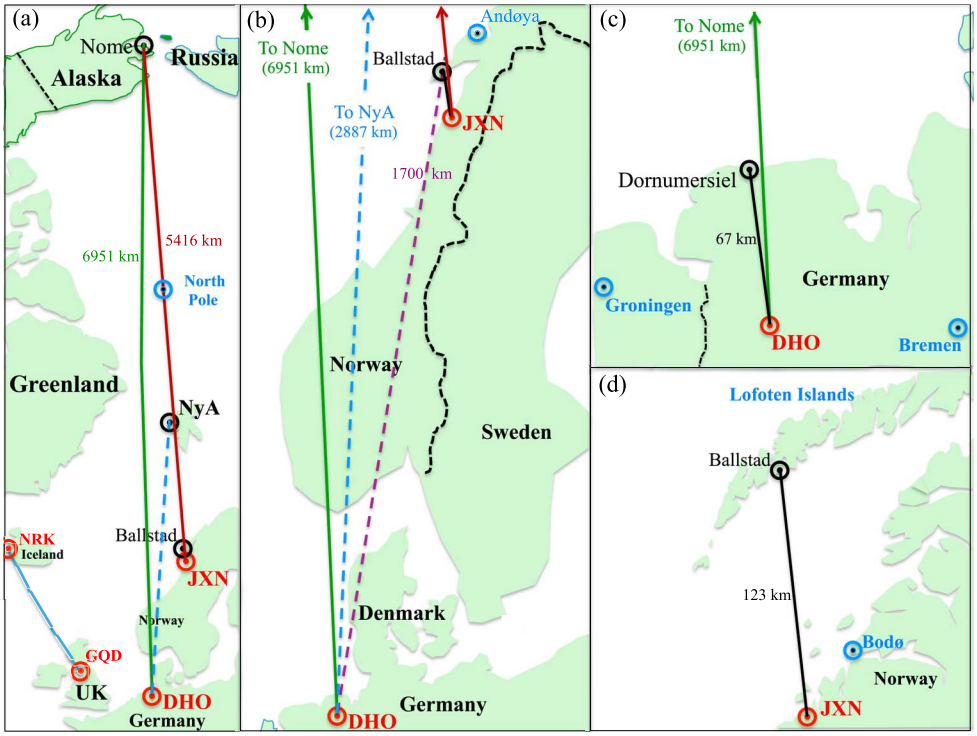

Figure 1. The VLF radio paths from transmitters DHO (23.4 kHz) and JXN (16.4 kHz) used here to find the Arctic lower *D* region parameters.

part of the path just north of DHO being nearer midlatitude rather than polar. We then show that any effect of sea ice on our polar path is likely to be negligible. Following this we compare our results with those of others, both in terms of propagation parameters and electron number densities, at heights of ~70 km.

2. The Principal Long Arctic Path: DHO (North Germany) to Nome (Alaska)

2.1. Background: The Path, the Transmitter, the Receiving Sites, and the Technique

VLF amplitudes and phases (in μs, relative to GPS 1-s pulses) of the 23.4-kHz transmitter, DHO, in North Germany, were measured with a portable loop receiver at several sites in and near Nome, Alaska, on six days from 31 May to 5 June 2013 (early summer, weak solar maximum, $F_{10.7}$~130 sfu) in the (Nome) morning and in the (Nome) evening, ~1700 UT and ~0500 UT, when the solar zenith angle along the path was fairly constant, being within ~±5° of ~70° (i.e., when the Sun was ~20° above the horizon). The amplitudes and phases near the transmitter also needed to be measured to determine the amplitude and phase changes along the path. These measurements were made with the portable loop receiver in and near Dornumersiel on the north coast of Germany, ~67 km nearly due north of DHO (see Figure 1c), on the six days 15–20 June 2013.

Most VLF transmitters are not fully phase stable; for example, the phase of DHO at midday on 5 June 2013 is unlikely to be the same as its phase at the same time on 15 June 2013 partly because of occasional unintended phase jumps at the transmitter and partly due to small frequency offsets at the transmitter from the nominal frequency. Also, in the case of DHO, the radiated power can vary somewhat from day to day. To correct for these effects, continuous amplitude and phase recordings of DHO at St. John's, NL, Canada, as shown in Figure 2, were used. The recorder is an "UltraMSK" receiver (http://ultramsk.com), measuring VLF phases relative to GPS 1-s pulses, modulo 90° (e.g., Thomson et al., 2017), and is part of the AARDDVARK network. This 4.2-Mm DHO-St. John's path is very stable near summer midday. DHO itself has a significant, though fairly stable, frequency offset, which has been partly compensated for by the St. John's recording frequency being set to 23,400.00006173 Hz (relative to GPS), that is, above 23.4 kHz by 61.73 μHz which is essentially the same as 1 cycle in every 4.5 hr, or 80° per hour. Inspection of the phase panels in Figure 2 shows that the actual frequency of DHO was slightly higher than the recording

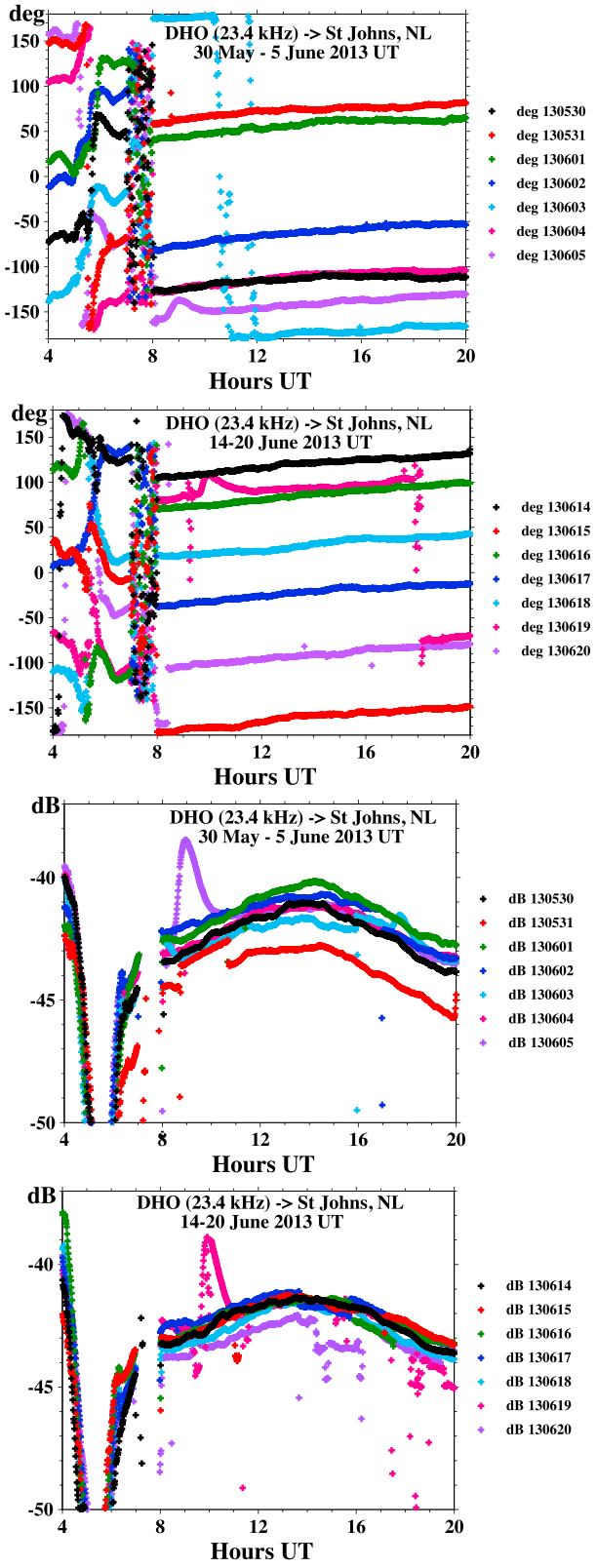

Figure 2. Phases and amplitudes of DHO, North Germany, recorded at St. John's, Newfoundland, to monitor DHO while the principal measurements were being made with a portable loop in Nome, Alaska, and Dornumersiel, Germany ("130530" = 30 May 2013, etc.).

frequency stated above by about 65° per day or 2.71°/hr in June 2013 (a small change in offset over ~2 years from the ~29°/day or ~1.2°/hr in July 2015 reported by Thomson et al. (2017)).

For both Nome and Dornumersiel, measurement sites were selected (within a few kilometers of each other) which were reasonably level and for which there appeared to be no significantly interfering power lines, radio transmitters, hills, tall buildings, buried conductors, etc. Each accepted site also needed to give rather consistent results within a horizontal distance of at least 5 m together with agreement with the other accepted sites after correcting the phase measurements at each site for the site's distance from the transmitter (at ~3.33 μs/km). While some initially selected sites needed to be rejected, most were able to be accepted, resulting in six accepted sites in Nome and five in Dornumersiel. From these sites, one in Nome, at 64.4966°N and 165.3774°W, and one in Dornumersiel, at 53.6720°N and 7.4741°E, were selected as representative or "principal sites" and used for calculating the path lengths, using the Vincenty algorithm (Vincenty, 1975; https://www.ngs.noaa.gov/cgi-bin/Inv_Fwd/inverse2.prl). The location of the transmitter, DHO, was taken as 53.0792°N and 7.6142°E (from Google Earth), giving the path distances DHO-Nome as 6,951.33 km and DHO-Dornumersiel as 66.62 km, and so the difference between these is 6,951.33–66.62 = 6,884.71 km, which is the distance associated with the phase difference measured between the principal sites in Nome and Dornumersiel. Although the DHO transmitter consists of several spaced towers with associated aerial wires, and so its center cannot readily be determined to better than a few hundred meters using Google Earth, this does not matter because Nome and Dornumersiel are in almost the same direction from DHO (~northward) and so the exact position of DHO has little effect on the Nome-Dornumersiel distance calculated above and used here for comparison with modeling calculations.

2.2. Measuring Phase Changes Along the Path

Determining the difference in phase between Nome and Dornumersiel at 23.4 kHz from the (principal site) observations is now described. At Nome the phase measurements were made 31 May–5 June 2013, while those at Dornumersiel, as indicated above, were made ~2–3 weeks later, 15–20 June 2013. The phase plots of DHO at St John's in Figure 2 record how the phase of DHO itself changed during this two- to three-week interval. Using the frequency offset of DHO (as discussed above) would not be appropriate alone because this would not be accurate enough for such a long period (two to three weeks) and, more importantly, it would take no account of DHO phase jumps during this period (and such jumps did occur particularly in the period 6–15 June). Instead, the DHO phase at St John's was read directly from the plots in Figure 2 at 16 UT on each measurement day and then the phase of DHO at the measurement times on a given measurement day was calculated from the preceding 16 UT phase, together with the frequency offsets above, over the just ~1–12 hr (from 16 UT) rather than over two to three weeks. The time 16 UT was chosen because the DHO-St. John's path was fairly near path midday (14 UT) and so rather stable, and also because it was reasonably close to the times of the actual phase readings at Nome (~05 UT and ~17 UT) and Dornumersiel (~12 UT).

Table 1
Phase Measurements and Adjustments for DHO (23.4 kHz), North Germany to Nome, Alaska

	Location/Details	UT 2013		μs	degrees	Recorder/Source
N1	**Nome, Alaska**	0439	5 June	18.6		Portable loop phase, as measured
N2	St. John's	1600	4 June		−107	Offset recorder phase, as recorded (Figure 2)
N3	St. John's	0439	5 June		17.3	Offset recorder, derived from N2 using time difference
N4	St. John's	0439	5 June		−110.7	Nonoffset recorder, relative to 0° at 1600, 31 May 2013, derived from N3
N5	Nome	0439	5 June	5.5		Portable loop, relative to nonoffset 0° at 0439, 5 June 2013 UT, from N1 and N4
N6	**Nome average, 31 May–5 June**			**5.29**		Average of 11 measurement sets similar to N5, each set near ~5 UT or ~1700 UT
D1	**Dornumersiel**	1323	15 June	15.3		Portable loop phase, as measured
D2	St. John's	1600	15 June		−156	Offset recorder phase, as recorded (Figure 2)
D3	St. John's	1323	15 June		17	Offset recorder derived from D2 using time difference
D4	St. John's	1323	15 June		−102	Nonoffset recorder, relative to 0° at 1600, 31 May 2013 UT, derived from D3
D5	Dornumersiel	1323	15 June	3.2		Portable loop, relative to nonoffset 0° at 1323, 15 June 2013 UT, from D1 and D4
D6	**Dornumersiel average, 15–20 June**			**3.35**		Average of six measurement sets similar to D5, each set near ~12 UT
	Nome-Dornumersiel			**1.94**		*Observed* average phase delay = 5.29–3.35 = 1.94 μs (Nome-Dornumersiel)
	Nome-Dornumersiel			16.20		*Free-space* delay (*d*/*c*, *d* from Vincenty) modulo DHO half-period (~21.37 μs)
	Nome-Dornumersiel			7.11	60	*Waveguide* delay = 1.94–16.20 + 21.37 = 7.11 (modulo 21.37 μs, DHO half-period)
	LWPC—phase at Dornumersiel				129	LWPC-calculated *waveguide* phase (relative to free space)
	Observed LWPC—phase at Nome				**−21**	=129°–60° = 69° ≡ −21° (modulo 90°), shown in top panel of Figure 3

The determination of the Nome-Dornumersiel phase difference at 23.4 kHz is now given in more detail. A summary can be found in Table 1. At Nome, at 0439 UT on 5 June 2013 UT, the portable loop receiver measured the phase delay of DHO as 18.6 μs (relative to GPS 1-s pulses). From Figure 2 the phase of DHO at 16 UT on 4 June was −107° on the St. John's recorder. From the DHO offset given above, 2.71°/hr, the recorder's phase at the time of the Nome measurement, 12.65 hr later, can be calculated as −107 + 90 + 2.71 × 12.65 = 17.3° (modulo 90°). Now this recorder, as explained above, is offset from 23.4 kHz by 80°/hr but, in contrast, the portable loop measures phases at exactly 23.4 kHz and so we need to convert the St. John's offset-recorder phases to exactly 23.4 kHz. For convenience, suppose we had also had a nonoffset recorder (i.e., measuring phase on exactly 23.4 kHz) at St. John's which, at (the arbitrarily chosen time of) 1600 UT on 31 May 2013 UT, recorded a phase of 77° (the same as for the actual offset recorder) for DHO. Then, at the time of the above Nome measurement, 4 × 24 + 12.65 = 108.65 hr later, the nonoffset-recorder phase would have advanced by 108.65 × 80 = 52° (modulo 90°) plus the phase change on the actual offset recorder, 17.3°–77°, and so this nonoffset recorder would have read 77° + 52° + (17.3°–77°) = 69.3° ≡ −110.7° (modulo 90°) while, as noted above, the portable loop at Nome was measuring the DHO phase delay as 18.6 μs. Thus, relative to 0° on this nonoffset recorder, the portable loop DHO-Nome phase delay would have been 18.6–(110.7/180) × 21.37 = 5.5 μs (where 180° and 21.37 μs correspond to half a period of 23.4 kHz). When this phase-normalization process (to 0° on the nonoffset recorder) was repeated for each of the other 10 (5 morning and 5 evening) DHO-Nome phase delays, 31 May–4 June 2013, an average DHO-Nome phase delay (for the 11 measurements, 31 May–5 June 2013 UT) of 5.29 μs was found (range 4.0–6.3 μs; details in the supporting information).

The DHO-Dornumersiel phase delay was similarly determined. At Dornumersiel, at 1323 UT on 15 June 2013 UT, the portable loop receiver measured the phase delay of DHO as 15.3 μs (relative to GPS 1-s pulses). From Figure 2 the phase of DHO at 16 UT on 15 June was −156° on the St. John's recorder. From the DHO offset given above, 2.71°/hr, the recorder's phase at the time of the Dornumersiel measurement, ~2.6 hr earlier, can be calculated as −156 + 180–2.71 × 2.6 = 17° (modulo 90°). At the time of this Dornumersiel measurement, 14 × 24 + 21.39 hr after 1600 UT on 31 May 2013 (the phase reference time chosen for Nome), the nonoffset recorder would have advanced by (14 × 24 + 21.39) × 80 = 61° (modulo 90°) plus the phase change on the actual offset recorder, 17°–77°, and so this nonoffset recorder would have read 77° + 61° + 17°–77° = 78° ≡ −102° (modulo 90°). Thus, for 0° on this nonoffset recorder, the portable loop DHO-Dornumersiel phase delay would have been 15.3–21.37 × 102/180 = 3.2 μs. When this process was repeated for each of the other 5 days, 16–20 June 2013, an average DHO-Dornumersiel phase delay (for the six measurement days, 15–20 June 2013) of 3.35 μs was found (range 3.0–3.7 μs; details in the supporting information).

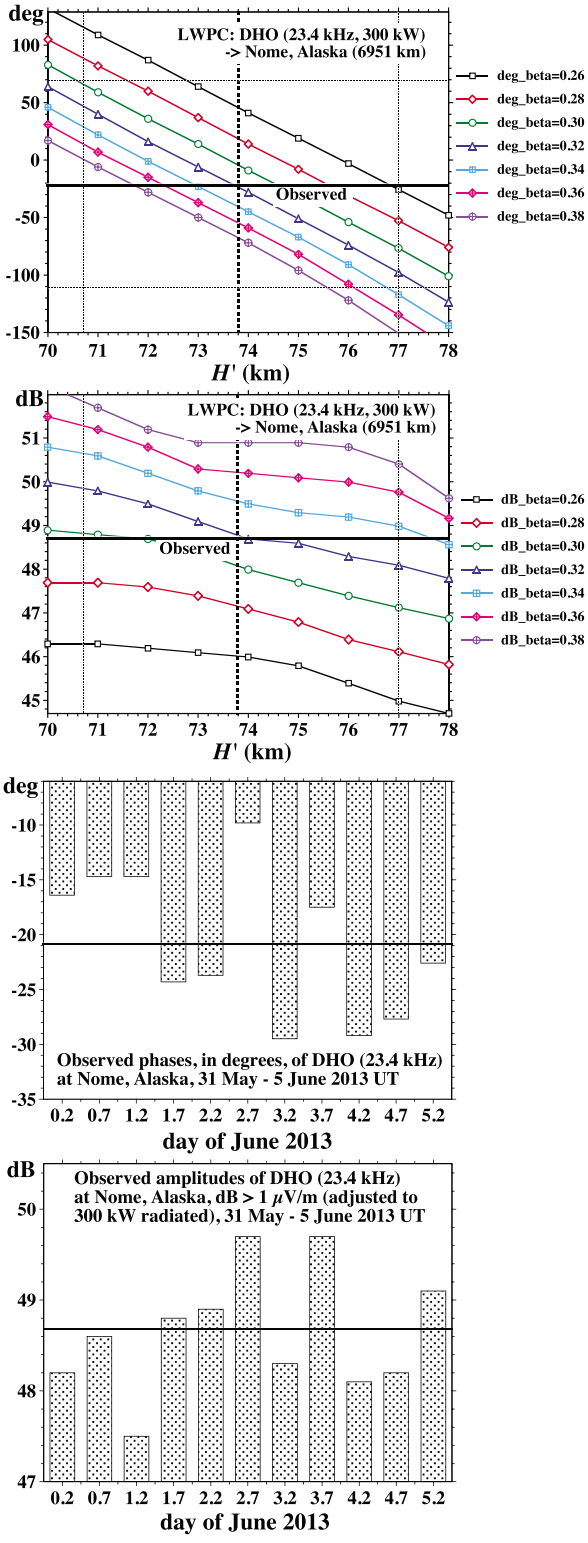

Figure 3. (top two panels) Calculations of the phase and amplitude of DHO (North Germany) at Nome, Alaska, using LWPC with a range of appropriate values of H' and β, compared with the averaged observations at Nome, 31 May–5 June 2013 UT. (bottom two panels) The observed phase and amplitude at each of the 11 measurement times, ~5 UT and ~17 UT on each of these six days, to illustrate the stability of the DHO-Nome polar path.

Because these average phase delays, DHO-Nome = 5.29 μs and DHO-Dornumersiel = 3.35 μs, are both referred to the same phase at DHO (using the St. John's recorded phases as proxies above), the phase delay difference for Dornumersiel-Nome is 5.29–3.35 = 1.94 μs (modulo a quarter period of 23.4 kHz = 0.25/0.0234 = 10.7 μs). VLF propagation codes, such as the U.S. Navy's ModeFinder and LWPC waveguide codes (Ferguson & Snyder, 1990; Morfitt & Shellman, 1976), use ionospheric *D* region models characterized by the height and sharpness parameters, H' and β (Wait & Spies, 1964), to calculate the phases and amplitudes at chosen receiver sites such as Nome and Dornumersiel. The differences between the calculated phases at these two sites, over a range of values of H' and β, can then be compared with the observed phase difference, with a match determining H' and β for the *D* region on the path. As is usual with propagation codes, LWPC calculates the phase change along the path relative to the free space, speed-of-light, path delay while the observed delay (1.94 μs here) includes both free-space and "waveguide" delays. The free-space delay is readily calculated from the Vincenty distance given above and the (exact) free-space speed of light: 6,884.71/0.299792458 = 22,964.92 μs ≡ 16.20 μs, modulo a half-period of 23.4 kHz. Thus, the observed waveguide delay is 1.94–16.20 + 21.37 = 7.11 μs, which is equivalent to 7.11 × 180/21.37 = 60°.

The LWPC-calculated phase at Dornumersiel is 129° (largely independent of H' and β because the ground wave is very dominant at such a short range). Hence, the observed 60° phase delay from Nome to Dornumersiel means the observed phase at Nome, in LWPC degrees, was 129°–60° = 69° ≡ −21° (modulo 90°). Figure 3 shows the LWPC-calculated phases and amplitudes (dB >1 μV/m for 300-kW radiated power) of DHO at Nome for various values of H' and β, together with the observed phase value shown as −21°.

2.3. Measuring DHO Amplitudes and Determining the Radiated Power of DHO

The amplitude of DHO now needs to be considered. DHO's radiated power is not as constant as most U.S. Navy transmitters and so some corrections are needed. For example, during the Nome measurement period (31 May–5 June 2013 UT), DHO was on reduced power by about 2.0 dB on 31 May and up to 0524 UT on 1 June. This can be seen in Figure 2 as well as in VLF recordings at other sites available on the BAS website (given in the Acknowledgements). The Nome amplitude values at these times were thus increased by 2.0 dB before averaging with the other Nome amplitudes resulting in 49.5 ± 0.3 dB > 1 μV/m, for the average of all the DHO amplitudes measured at Nome around 05 UT and 17 UT each day. At Dornumersiel, the average observed amplitude, 15–20 June 2013, was 98.1 dB (>1 μV/m) after increasing the amplitudes measured on 20 June (all before 12 UT) by 1.0 dB in line with the recorded amplitude at St. John's on that day, and similarly increasing those on 18 June by 0.5 dB. LWPC calculates that DHO was radiating ~0.4 dB above 300 kW to give this observed 98.1 dB (>1 μV/m) amplitude at Dornumersiel. Inspection of the two amplitude panels in Figure 2 shows that the average amplitude during the Nome measurement period was ~0.4 dB higher than during the Dornumersiel measurement period (after the above 0.5–2.0-dB corrections were applied). This means the 49.5-dB amplitude at Nome corresponds with DHO radiating ~0.8 dB above 300 kW. Hence, the observed

amplitude line in Figure 3 is at 49.5–0.8 = 48.7 dB so that both the observed and calculated amplitudes in Figure 3 are for 300 kW radiated.

2.4. Comparing Observations With Calculations: Determining Arctic Values of H' and β

As can be seen in Figure 3, there is a good match between the observed phase and amplitude of DHO at Nome with the corresponding LWPC-calculated values for H' = 73.8 km and β = 0.32 km^{-1}. However, it needs to be remembered that the observed phase is modulo 90°. This occurs because the nature of MSK modulation is such that there is an inherent 180° ambiguity on each of its two constituent frequencies (23.35 and 23.45 kHz for DHO's 200 baud MSK on 23.4 kHz), which means there is always at least an inherent 180° ambiguity for both portable loop phases and recorder phases. In addition, our recorder combines the two sideband phases internally so that if only one jumps 180°, the recorded output will jump 90° (e.g., Thomson et al., 2017). Hence, in the phase panel of Figure 3, there are two horizontal dotted lines 90° on either side of the bold solid line at −21°, and from these, using both the phase and amplitude panels, it can be seen that there are also possible matches for H' = 70.7 km and β = 0.30 km^{-1} and for H' = 77.0 km and β = 0.335 km^{-1}. In the next two sections, it will be shown that the bolded lines giving the first good match given above, H' = 73.8 km and β = 0.32 km^{-1}, are the very much more probable solution.

3. Solar Zenith Angle Effects at Higher Latitudes: Subarctic Paths

As mentioned in section 1, the increasing intensity of galactic cosmic rays at *D* region heights, in moving from low latitudes (Thomson et al., 2014; ~20°N) toward high latitudes (Thomson et al., 2017; ~53°N), has been observed to reduce the daytime solar zenith angle (SZA) dependence of H' and β. In addition, generation of *D* region electrons by energetic particle precipitation can be expected to be much greater in polar regions than at lower latitudes. Thus, the SZA dependence of H' and β can be expected to correspondingly decrease toward the polar regions not only because of these effects but also because the higher SZAs at higher latitudes result in solar Lyman α having a reduced effect on the *D* region.

A measure of the extent of this dependence was able to be observed using VLF phase and amplitude recordings from two subarctic paths: (1) NRK (37.5 kHz, Grindavik, Iceland; 63.8504°N, 22.4668°W) to Eskdalemuir (55.313°N, 3.207°W) and (2) GQD (22.1 kHz, Skelton, England; 54.7319°N, 2.8832°W) to Reykjavik, Iceland (64.1°N, 21.8°W). The paths are fairly similar in position (see Figure 1a) but they are in opposite directions and on rather different frequencies. The NRK-Eskdalemuir recordings are from June 2015 because of recorder or transmitter difficulties in 2013 and 2014, while the GQD-Reykjavik recordings are from June 2013, near the times of the DHO-Nome transarctic measurements reported here.

The VLF results from these two subarctic paths are shown in Figure 4, where the panels on the left are for NRK-Eskdalemuir (~1,435 km) while those on the right are for GQD-Reykjavik (~1,490 km). The top four panels show approximately two-week averages of the observed phase and amplitude changes during daytime, as the SZA changes by ~45° between ~82° near dawn/dusk to 37° at path midday. These changes, ~5°–10° in phase and <~0.5 dB in amplitude, are quite small compared with lower latitude paths (e.g., Thomson et al., 2014, 2017). The lower four panels of Figure 4 show the phases and amplitudes, as colored lines, for the two paths as calculated by U.S. Navy code LWPC for appropriate ranges of H' and β. Superposed on these are the observed changes in phase and amplitude, over the time interval 0500–2030 UT (SZA (37°–82°)), from each of the corresponding top four panels, to determine the changes in H' and β during this period. Note that measured absolute phases and amplitudes for these two subarctic paths were not available so that the (midday) values of H' and β needed to be estimated by extrapolating from previous results from a slightly lower latitude (Thomson et al., 2017). This is probably only of marginal importance in determining the changes in H' and β here because, as can be seen in the lower four panels of Figure 4, it is the changes in phase and amplitude that mainly determine the changes in H' and β; these latter changes are not greatly affected by whether the midday H' is taken as (say) 73 or 73.5 km.

Thus, from the lower four panels in Figure 4, it can be seen that there is an increase in H' of ~1.3 km for NRK-Eskdalemuir in 2015 and an increase of ~1.7 km for GQD-Reykjavik in 2013 when the SZA increased by ~45° from 37° at path midday at 1245 UT to ~82° at 0500/2030 UT near dawn/dusk. The solar cycle galactic cosmic ray intensity variation at the Earth appears to lag sunspot number by ~9–12 months (Forbush, 1958; Neher & Anderson, 1962). At the (weak) solar maximum of the current solar cycle, the (ISES/NOAA) smoothed sunspot

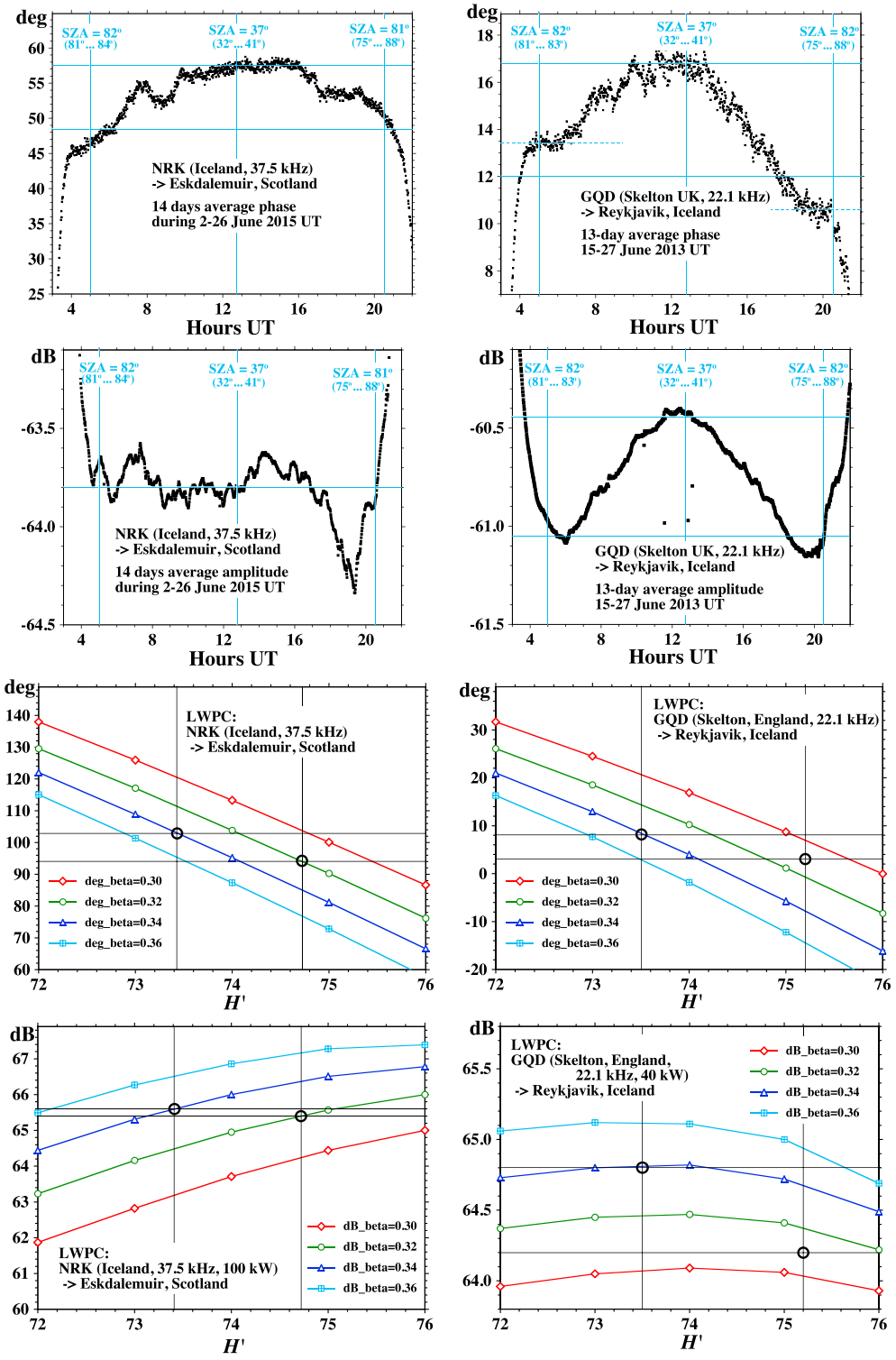

Figure 4. Changes of phase and amplitude with solar zenith angle (SZA) on two subarctic VLF paths: (left four panels) NRK, Iceland, to Eskdalemuir, Scotland and (right four panels) GQD, Skelton, England, to Reykjavik, Iceland. The top four panels are the observations from the VLF recordings. The bottom four panels show LWPC-calculated phases and amplitudes as functions of H' and β for the paths compared with the observed changes in phase and amplitude from the top four panels (see text for more details).

number was ~60 from mid-2012 to mid-2014 but had reduced to ~40 in mid-2015. While the corresponding lower cosmic ray intensity in 2013 might account for the larger SZA variation in H' in 2013 (1.7 km) than in 2015 (1.3 km), the considerable day-to-day scatter in the VLF measurements at these subarctic latitudes means it could also be just statistical error. The change in H' with SZA at these subarctic latitudes is probably best estimated as ~1.6 km for a 45° change in SZA. In comparison, on an ~5° lower latitude path, DHO to Eskdalemuir, Thomson et al. (2017) found H' changed (in their Figure 6) by ~4 km for a 45° change in SZA. These small changes with SZA in the high-latitude *D* region are consistent with the near constant rocket-measured electron densities of Danilov et al. (2003), 75 km above Heiss Island (~80°N, ~58°E; geographic), in the SZA range 67°–80°. For SZA $>$ 80° their electron densities start to change more rapidly with SZA just as our VLF plots in Figure 4 do (while for SZA $<$ ~67° they display no data). This reduction in the change in H' with SZA with increasing latitude could be consistent with increasing galactic cosmic ray intensity with increasing latitude and the reducing affect of solar Lyman α due to the decreasing SZA with increasing latitude. It would also be consistent with a higher proportion of the *D* region electrons at high latitudes being generated by energetic particle precipitation.

This also has clear implications for choosing between the three possibilities for H' and β in Figure 3 for the DHO-Nome path—that is, for resolving the 90° phase ambiguity. If H' = 77 km (with β = 0.335 km^{-1}) were the correct choice, this would match very nicely with the plot of the variation of H' with SZA for the DHO-Eskdalemuir path (discussed in the previous paragraph). However, such a match would also imply that the polar path was strongly SZA dependent (i.e., also being dominated by SZA dependent solar Lyman α production) which, in turn, would imply that the subarctic paths in between (NRK-Eskdalemuir and GQD-Reykjavik) were also strongly SZA dependent, but the results of Figure 4 clearly show they are not. Thus, the H' = 77 km option for DHO-Nome in Figure 3 must be rejected. The third possible choice of H' = 70.7 km (with β = 0.30 km^{-1}), in Figure 3 for DHO-Nome, also seems unlikely because it would be a long way below a height at which solar Lyman α could penetrate (at the high SZA of ~70°) and create an SZA dependence, whereas, in reality, there appears to be a comparatively gradual reduction in SZA dependence with increasing latitude from the mid-high-latitude DHO-Eskdalemuir path through to the subarctic NRK-Eskdalemuir and GQD-Reykjavik paths. Thus, the middle choice, H' = 73.8 km and β = 0.32 km^{-1}, in Figure 3, for DHO-Nome is most likely the correct choice.

4. The Long Arctic Path: JXN (Norway) to Nome (Alaska)

Similar phase and amplitude measurements of the 16.4-kHz transmitter, JXN on the west coast of Norway at ~67°N, were made in Nome, Alaska, using the same portable loop system at the same times and places as the DHO measurements. As can be seen in Figure 1a, the 5416-km path passes almost over the North Pole and the AARDDVARK recording site at Ny-Ålesund (NyA) in Spitsbergen. The phases and amplitudes near the transmitter were measured with the portable loop receiver (as for DHO) in and near Ballstad on Norway's Lofoten Islands, ~123 km approximately due north of JXN (Figure 1d), on the four days 9–12 June 2013 UT. JXN is essentially amplitude and phase stable, having negligible permanent frequency offset; in these regards it behaves more like a U.S. Navy VLF transmitter rather than like DHO. However, unlike DHO and the U.S. Navy transmitters, JXN often does not transmit continuously. Fortuitously, however, it mainly did so during the period 31 May–3 June 2013 when most of the Nome measurements were being made. Often, and in particular, during the Ballstad measurements and the remainder of the Nome measurements here (4–12 June 2013), the JXN transmitter was on for periods of just 1 hr, 6 times a day, beginning 0, 4, 8, 12, 16, and 20 UT. Details can be seen in Figure 5 where, as for DHO, recordings of JXN at St. John's, Canada, were used to check and correct for any phase jumps and (minor) phase drifts.

The JXN antenna consists of a wire strung between two mountains fed by an up/down lead to the transmitter hut below. JXN's location was taken as 66.9822°N and 13.8737°E. Due to the difficulties of determining the effective center of the antenna, this could be in error by several hundred meters or more but, as for the exact location of DHO in section 2, this does not matter because both Ballstad and Nome are very nearly in the same direction (north) from JXN. This JXN location gives the Vincenty distance to Nome as 5,416.22 km and the Vincenty distance to Ballstad (principal site; 68.0745°N, 13.5563°E) as 122.57 km.

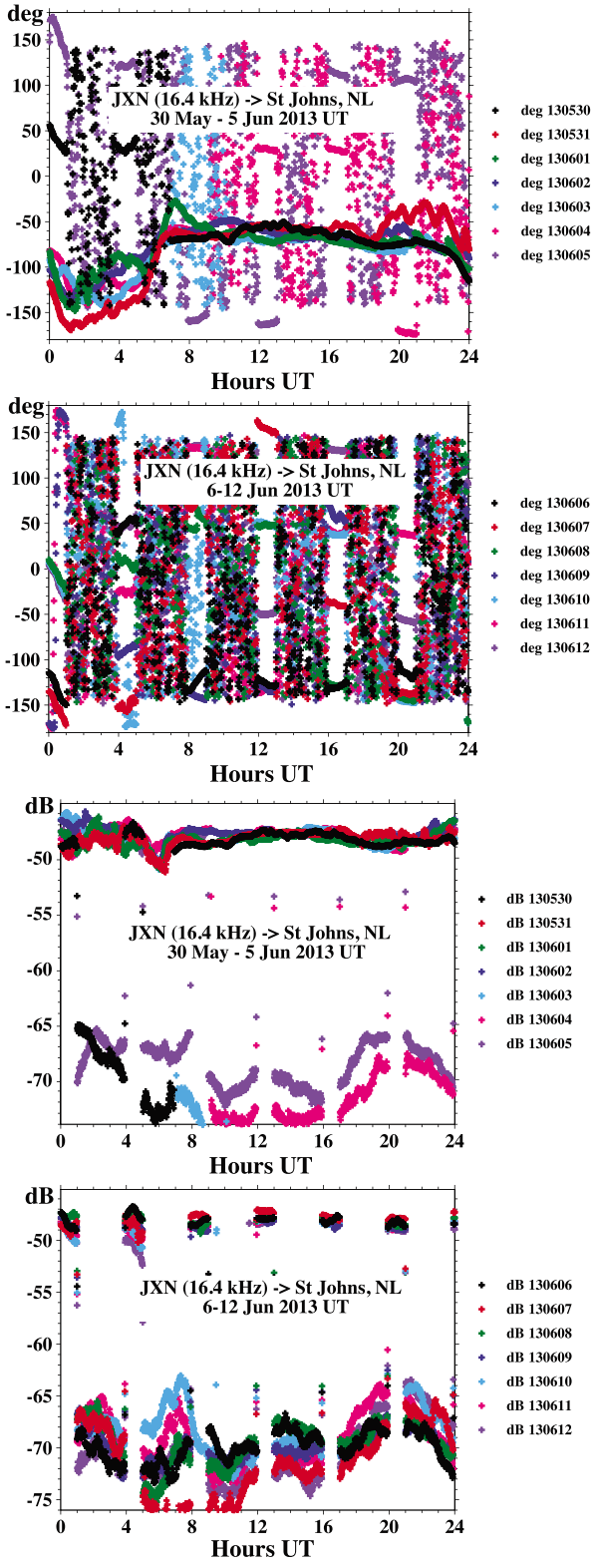

Figure 5. Phases and amplitudes of JXN, Norway, recorded at St. John's, Newfoundland, to monitor JXN while the principal measurements were being made with a portable loop in Nome, Alaska, and Ballstad, Norway. During the period ~ 4–12 June 2013 JXN is on-air for just six 1-hr periods per day (starting 0, 4, 8, 12, 16, 20 UT).

The determination of the observed Nome-Dornumersiel phase difference at 16.4 kHz is now described. A summary is given in Table 2. At Nome, at 0454 UT on 1 June 2013 UT, the portable loop receiver measured the phase delay of JXN as 7.3 μs (relative to GPS 1-s pulses). Figure 5 shows, that on 1 June (12–17 UT), JXN's phase at St. John's was −72° ≡ 18° (modulo 90°). Thus, relative to a JXN phase of 0° at St. John's, the phase delay at Nome would have been 7.3 + (18/180) × 30.49 = 10.3 μs (where 30.49 μs and 180° correspond to half a period of 16.4 kHz). When the other 10 portable loop JXN phase delays at Nome were similarly corrected to 0° at St. John's, an average JXN-Nome phase delay (for the 11 measurements 31 May–5 June 2013 UT) of 10.72 μs was found (range 9.7–13.5 μs; details in the supporting information). At the principal site at Ballstad, at 1602 UT on 10 June 2013 UT, the GPS-referenced portable loop measured JXN's phase as 16.3 μs. For the Ballstad area only, the position-corrected average of the phase delays at the other four measurement sites (within 6–7 km) proved to be larger over the four measurement days (9–12 June 2013) by a small but nonnegligible amount. This meant it was appropriate to increase the Ballstad principal site phases by ~0.64 μs, thus increasing the 16.3 μs above to 16.94 μs (to represent an average of all five sites). From Figure 5 on 10 June (12–17 UT), JXN's phase at St. John's was 43° ≡ −47° (modulo 90°). Thus, relative to a JXN phase of 0° at St. John's, the phase delay at Ballstad was 16.94–47/180 × 30.49 = 9.0 μs. When the other portable loop phase delays at Ballstad were similarly adjusted for 0° at St. John's, an average JXN-Ballstad phase delay (for 9–12 June 2013) of 9.35 μs was found (range 7.7–11.0 μs; details in the supporting information). Hence, the phase delay difference for Ballstad-Nome is 10.72–9.35 = 1.37 μs (modulo a quarter period of 16.4 kHz = 0.25/0.0164 = 15.24 μs). The free-space delay from the JXN Vincenty distances given above is (5,416.22–122.57)/0.299792458 = 17,657.72 ≡ 5.27 μs, modulo a half-period of 16.4 kHz. Thus, the observed waveguide delay is 1.37 + 15.24–5.27 = 11.34 μs, which is equivalent to 180 × 11.34/30.49 = 67°.

ModeFinder (slightly to be preferred to LWPC for a short path with virtually no land) calculated the phase for JXN at Ballstad as 48° (using H' = 73 km and β = 0.32 km^{-1}). The observed 67° phase delay from Nome to Ballstad means the observed phase at Nome, in LWPC degrees (=ModeFinder degrees +90°), was 48°–67° = −19° (modulo 90°). Figure 6 shows the LWPC-calculated phases and amplitudes (in dB >1 μV/m for 50-kW radiated power) for JXN at Nome for appropriate values of H' and β, together with the observed phase of −19°. Because of the amplitude measurement difficulties for JXN at Ballstad discussed below, the value of β from the DHO-Nome plot (Figure 3; ~0.32 km^{-1}) has been used in Figure 6 together with the observed JXN-Nome phase of −19°, resulting, as can be seen, in H' = 73.9 km for JXN-Nome, which is close to the DHO-Nome value of 73.8 km.

The average amplitude measured for JXN at the sites near Ballstad with the portable loop was 80.7 dB > 1 μV/m. This was unexpectedly low—about 4 dB lower than expected for JXN radiating 50 kW from ~123 km away. Comparisons of the relative daytime amplitudes of JXN, DHO, and NAA at St. John's (allowing appropriately for propagation and for the plane of the loop being oriented 76°E of N) had resulted in a fairly good estimate of 50 kW for JXN. It was then noticed that the amplitudes of DHO at the same sites near Ballstad were also low by very nearly the same 4 dB. While it might appear that this could be due to a (temporary) fault in the

Table 2
Phase Measurements and Adjustments for JXN (16.4 kHz), Norway to Nome, Alaska

	Location/Details	UT 2013		μs	degrees	Recorder/Source
N1	**Nome, Alaska**	0454	1 June	7.3		Portable loop phase, as measured
N2	St. John's	12–17	1 June		−72	Recorder phase, as recorded (Figure 5)
N3	Nome	0454	1 June	10.3		Portable loop, relative to 0° at recorder, derived from N1 and N2
N4	**Nome average, 31 May–5 June**			**10.72**		Average of 11 measurement sets similar to N3, each set near ~5 UT or ~1700 UT
B1	**Ballstad, Norway**	1602	10 June	16.94		Portable loop phase, as measured (see text in section 4)
B2	St. John's	12–17	10 June		43	Recorder phase, as recorded (modulo 90°; Figure 5)
B3	Ballstad	1602	10 June	9.0		Portable loop, relative to 0° at recorder, derived from B1 and B2
B4	**Ballstad average, 9–12 June**			**9.35**		Average of four measurement sets similar to B3, each set ~8–17 UT
	Nome-Ballstad			**1.37**		*Observed* average phase delay = 10.72–9.35 = 1.37 μs (Nome-Ballstad)
	Nome-Ballstad			5.27		*Free-space* delay (*d*/*c*, *d* from Vincenty) modulo JXN half-period (~30.49 μs)
	Nome-Ballstad			11.34	67	*Waveguide* delay = 1.37–5.27 + 15.24 = 11.34 (modulo 15.24 μs, JXN 1/4 period)
	ModeFinder-phase at Ballstad				48	ModeFinder-calculated *waveguide* phase (relative to free space)
	Observed LWPC—phase at Nome				**−19**	=48°–67° = −19° (modulo 90°), shown in top panel of Figure 6

portable loop, it is felt that this is unlikely. The loop has never shown such a problem and has had similar field use over many years both before and after Ballstad. Although unconfirmed, a more likely explanation is the terrain which is low-conductivity ground, 0.001 S/m (International Telecommunications Union, 1999; Morgan, 1968) in the form of closely spaced islands (the Lofoten Islands) akin to a peninsula in a conducting sea (4 S/m) with many rather small seawater inlets. The VLF radio waves induce currents in the ground (or sea) which contribute to the magnetic fields measured by the portable loop. These currents normally flow uniformly across the ground, but if deflected away to nearby high-conductivity (seawater) paths, this can leave a deficit in the low-conductivity ground below the loop antenna and so give low readings. At Ny-Ålesund, 1,334 km to the north of JXN, comparison of the amplitudes of JXN (68.8 dB $>$ 1 μV/m) and DHO (65.0 dB $>$ 1 μV/m) recorded on the loop antenna (after allowing for the loop plane being oriented 145°E of N) with LWPC calculations (H' = 74 km and β = 0.32 km^{-1} for JXN and H' = 73 km and β = 0.33 km^{-1} for DHO) imply that, at least in the direction of Ny-Ålesund (i.e., north), JXN was radiating ~2 dB above 50 kW in June 2013. While the error on this estimate may be as high as 1–2 dB, it does imply that, at least to the north and so toward Nome, the effective radiated power of JXN may well have been ~0.5 dB above 50 kW and so, when the observed amplitude at Nome (52.5 dB $>$ 1 μV/m) is corrected (back to 50 kW) for this, the observed amplitude at Nome becomes 52.0 dB, which as can be seen in Figure 6 (lower dashed horizontal line) would give values of H' and β for JXN-Nome very similar to those for DHO-Nome (in Figure 3), that is, H' = 73.8 km and β = 0.32 km^{-1}. The JXN-Nome results thus provide further support that the 90° phase ambiguity for DHO-Nome in Figure 3 was correctly resolved as H' = 73.8 km and β = 0.32 km^{-1}.

Of course, the fact that the amplitude of JXN measured at Ballstad was much lower than expected (~4 dB) casts doubt on the accuracy of the JXN-Nome measurements compared with the DHO-Nome measurements where there were no such issues. In particular, the low amplitude of JXN at Ballstad may cast doubt on the phase measurements of JXN at Ballstad. However, the mechanism for the low amplitudes suggested above would likely not greatly affect the phases. In particular, as noted above, the DHO amplitude was also low by a very similar amount but, as shown in the supporting information, the observed phase of DHO at Ballstad (in LWPC degrees) was −0.4° only ~7.5° higher than the phase calculated by LWPC (using H' = 73 km and β = 0.34 km^{-1}). Hence, the JXN-Nome results reported here are very likely to have sufficient accuracy to independently resolve the 90° phase ambiguity for the DHO-Nome results and so are important; however, the uncertainties associated with the JXN-Nome results mean that averaging them with the DHO-Nome results would not likely improve the overall Arctic accuracy over using the DHO-Nome results (H' = 73.8 km and β = 0.32 km^{-1}) alone.

5. Discussion, Summary, and Conclusions

5.1. Adjustment for the Small Mid-Latitude Part of the DHO-Nome Path

In section 3, two subarctic paths, NRK-Eskdalemuir and GQD-Reykjavik, between ~55° and 64° geographic latitudes, were discussed and found to vary relatively little with solar zenith angle during daylight

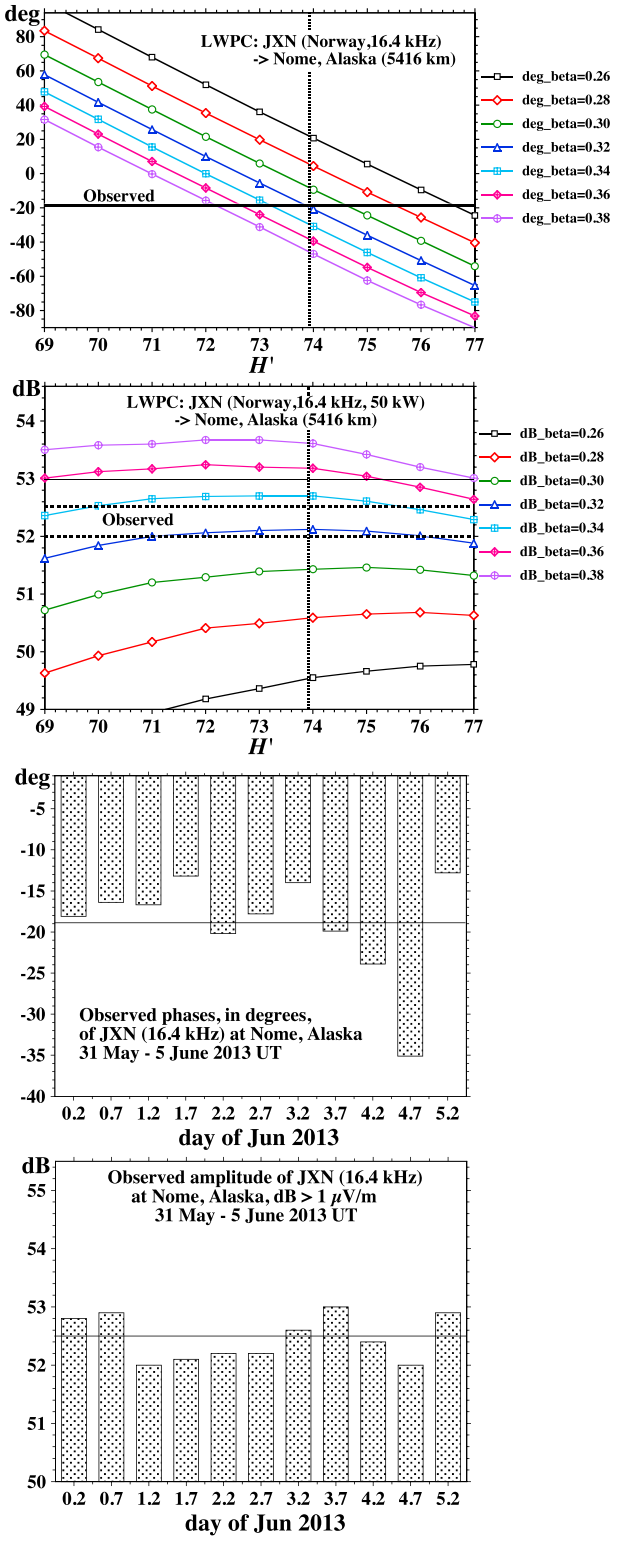

Figure 6. (top two panels) Calculations of the phase and amplitude of JXN (Norway, ~67°N) at Nome, Alaska, using LWPC with a range of appropriate values of H' and β, compared with the observations at Nome, 31 May–5 June 2013 UT. (bottom two panels) The observed phase and amplitude at each of the 11 measurement times, ~5 UT and ~17 UT on each of these 6 days, to illustrate the stability of the JXN-Nome polar path.

compared with paths at lower latitudes, in particular with DHO-Eskdalemuir, ~53°–55°, implying that above ~60° latitude (at least at these longitudes ~0°), the lower ionospheric *D* region is not dominated by solar radiation (such as Lyman α) but rather, at least during quiet times, by galactic cosmic rays or energetic particle precipitation. It thus seems reasonable to consider the *D* region above ~60° as the Arctic or polar *D* region. This means that the DHO-Nome path measured here contains a small part (10–12%) which is transitioning from DHO-Eskdalemuir (high mid-latitude) parameters, where H' ~76 km at SZA ~70° (Thomson et al., 2017) at the measurement times, ~05 UT and ~17 UT, to ~73.8 km for the whole (mainly polar) path, which implies that for the polar region alone H' = 73.7 km, which is a rather minimal adjustment. The corresponding adjustment for β would be <0.003 km^{-1} and so can be neglected.

Hence, the daytime *D* region (Wait) height and sharpness parameters in the Arctic are here found to be $H' = 73.7 \pm 0.7$ km and $\beta = 0.32 \pm 0.02$ km^{-1} in the summer of 2013—that is, at (weak) solar maximum, $F_{10.7}$~130 sfu.

5.2. Possible Effects of Sea Ice on the Arctic VLF Propagation

As mentioned in section 1, Arctic sea ice thickness has been reported to average about 2 m in recent years. Even though the (horizontal/latitudinal) extent of the sea ice is quite strongly seasonally dependent, this thickness is not highly seasonally dependent (e.g., Kwok & Rothrock, 2009).

Because such relatively thin ice (~2–4 m) was not expected to have much measurable effect on VLF propagation, the U.S. Navy codes, LWPC and ModeFinder (used here), do not have direct provision for allowing for such thin ice. Specifically, although the codes allow for a very wide range of conductivities for the ground/ice/ocean on the lower boundary of the waveguide, they do not allow for this conducting layer thickness being less than the skin depth. However, it is, none-the-less, possible to make some reasonable estimates using the existing codes.

The sea ice can be conveniently thought of as fitting approximately into two categories: (new) first-year ice which has formed on the ocean over the preceding winter and (old) multiyear ice which has survived one or more summer melts. Their electrical conductivities are rather different because the first-year ice still contains much salty water compared with the multiyear ice where the salty water has mainly drained away. McNeill and Hoekstra (1973) reported resistivity measurements on these two types of ice. While in both cases the resistivity (and so the conductivity) varied with depth (up to ~1–3 m), reasonable average conductivity approximations from their measurements for ~2 m of ice for the present purpose are σ = ~0.03 S/m for first-year ice and σ = ~0.0003 S/m for multiyear ice. Both ModeFinder and LWPC show that for the long (transpolar) paths here, only the first-order waveguide mode is important; so we need consider the effect of the (thin) ice here only on the first-order mode.

ModeFinder gives the attenuations of the first-order mode for σ = ~0.03 and 4 S/m (seawater), as 2.76 and 2.51 dB/Mm, respectively, a difference of 0.25 dB/Mm. ModeFinder effectively assumes that the conducting layers have infinite thickness. In the case of the σ = ~0.03-S/m layer, the skin depth (at 23.4 kHz, DHO's frequency) is ~19 m, so the attenuation excess relative to seawater for just 2 m of ~0.03 S/m ice can be estimated as $0.25 \times 2/19 = 0.026$ dB/Mm. For σ = ~0.0003 S/m, ModeFinder gives the first-order mode attenuation as 8.0 dB/Mm, which is greater than that for

seawater by 8.0–2.5 = 5.5 dB/Mm, but for σ = ~0.0003 S/m, the skin depth is ~190 m so that the excess attenuation for 2 m of ~0.0003 S/m ice can be estimated as 5.5 × 2/190 = 0.055 dB/Mm. Recent Arctic ice extent maps imply that our signals will pass over up to ~ 4 Mm of sea ice with about two thirds being first year ice and the rest being multiyear ice (Perovich et al., 2017; Tschudi et al., 2016). This implies ~4 × (2 × 0.026 + 0.055)/3 = 0.14 dB of attenuation due to the sea ice which is effectively negligible relative to our previous error estimates.

For the phase velocity of the first-order mode (with respect to the speed of light, 300 m/μs), ModeFinder calculates 0.997523 and 0.997610 for σ = ~0.03 and 4 S/m, respectively, giving a phase velocity difference of 8.7×10^{-5} which for just 2 m of ~0.03 S/m ice reduces (as for the attenuation above) to $2/19 \times 8.7 \times 10^{-5} = 9.2 \times 10^{-6}$, which is equivalent to a phase delay (relative to seawater) of $10^6/300 \times 9.2 \times 10^{-6}$ = 0.031 μs/Mm or $0.031 \times 10^{-6} \times 23400 \times 360$ = 0.26°/Mm. For σ = ~0.0003 S/m, ModeFinder gives the corresponding first-order mode phase velocity as 0.996904, which is less than that for seawater by 0.997610–0.996904 = 70.6×10^{-5} which for 2 m of ~0.0003 S/m ice (skin depth 190 m) reduces to $2/190 \times 70.6 \times 10^{-5} = 7.4 \times 10^{-6}$, which is equivalent to a phase delay (relative to seawater) of $10^6/300 \times 7.4 \times 10^{-6}$ = 0.025 μs/Mm or $0.025 \times 10^{-6} \times 23400 \times 360$ = 0.21°/Mm. This implies ~4 × (2 × 0.26 + 0.21)/3 = 0.97° ≈ 1° of phase due to 4 Mm of sea ice which is again effectively negligible relative to our previous error estimates.

5.3. Comparison With Other VLF Measurements and Recommendations

Morfitt (1977), in a U.S. Navy NOSC report, suggested that appropriate lower *D* region parameters for VLF in daytime at high latitudes in summer were in the ranges H' = 72–74 km and β = 0.25–0.30 km^{-1} but emphasized that many more measurements were needed. A slightly more recent U.S. Navy NOSC report (Ferguson, 1980) recommended H' = 72.0 km and β = 0.30 km^{-1} at high latitudes in daytime; this recommendation was also made by the Comité Consultatif International des Radiocommunications (1990).

5.4. Comparison With MF Radar and Rocket Electron Densities at Andøya (69°N) Norway

Singer et al. (2011) have reported extensive electron density measurements overhead from the polar island of Andøya, Norway, at a latitude of 69°N in the *D* region using partial reflections from a 50-kW effective peak power, MF (3.19 MHz) radar. They show that their results are in good agreement with corresponding rocket-borne radio wave propagation measurements. Their increase of electron density with height profiles (in particular, their Figures 4, 11, and 16) are very similar to Wait profiles providing support for our use of Wait (H' and β) profiles in the Arctic. In order to compare their results more quantitatively with ours, our DHO-Nome VLF Arctic H' and β parameters determined here need to be converted into electron densities. To minimize the need to accurately know both the electron neutral collision frequency, ν, and the electron density, N_e, Wait introduced the parameter $\omega_r = \omega_o^2/\nu$ (e.g., Wait & Spies, 1964), where ω_o is the angular (electron) plasma frequency; hence, $\omega_r \approx 3{,}183\ N_e/\nu$ (since $e^2/\varepsilon_o m_e \approx 3183$). The advantage is that VLF propagation in the *D* region turns out to be largely a function of ω_r—if, for example, both N_e and ν are doubled (or both halved), there is very little effect on the propagation compared with doubling (or halving) ω_r itself. Wait defined the height at which $\omega_r = 2.5 \times 10^5$ rad/s as H', and ω_r was taken to vary with height, h, as $\omega_r = 2.5 \times 10^5 \exp(h - H')\beta$, thus defining β as a (near) constant with height, but varying with latitude, time of day, and solar cycle. This has been found to be a reasonable approximation since (1) the collision frequency is fairly nearly proportional to the neutral density which decreases nearly exponentially with height and (2) electron densities measured from other sources (e.g., rocket profiles) generally increase exponentially, at least approximately, with height. This has proved to be a very useful approximation for characterizing the *D* region for VLF propagation under a wide variety of conditions, both quiet and disturbed, including allowing quantitative analysis of geophysical perturbations.

To obtain electron densities from the above formulae and the H' and β values determined from VLF propagation measurements (such as DHO-Nome above), appropriate numerical values of the electron-neutral collision frequency, ν, are needed. VLF propagation codes including ModeFinder and LWPC use the Appleton-Lassen (Appleton-Hartree) formulation which assumes that the electron-neutral collision cross section is independent of velocity and so the collision frequency itself is proportional to (electron) velocity. About the time the predecessors of ModeFinder and LWPC were being coded, measurements were reported by Phelps and Pack (1959) and Pack and Phelps (1961), which indicated that, at the relevant energies, the

electron-N_2 collision cross section was not independent of velocity but proportional to it. This gave rise to a significantly more complicated magneto-ionic formulation (Sen & Wyller, 1960a, 1960b), simplified somewhat by Budden (1965). The architects of ModerFinder, LWPC, and their forerunners were aware of this but apparently chose to stay with the Appleton-Lassen formulation due to doubts about the extent of the velocity dependence, about the extent of its effects on the results of the calculations and about the computational complexities (extra integrals to evaluate), including likely computation speed. Budden (1988) clearly had some concerns about the range of velocities for the electron-N_2 cross-section proportionality with velocity, because zero velocity could imply zero cross section. However, additional measurements by Aggarwal et al. (1979) and calculations by Friedrich et al. (1991) are strongly suggestive that, while the electron-N_2 collision cross section may be only approximately proportional to the electron velocity, the Sen and Wyller (1960a, 1960b) formulation is likely to be more appropriate at least at MF wave frequencies.

Deeks (1966) made calculated comparisons at VLF of Appleton-Lassen and Sen-Wyller results and concluded (as Sen and Wyller had previously for higher frequencies) that the Appleton-Lassen results could be fairly satisfactory provided the collision frequency used in the Appleton-Lassen equations was greater by an appropriate factor of between 1.5 and 2.5 than the (easily calculable) monoenergetic collision frequency, ν_m. At altitudes below which $\nu_m >> \omega_H$ (the angular electron gyrofrequency, which is close to 10^7 rad/s in the polar *D* region), the appropriate factor was 1.5 while at altitudes above which $\nu_m << \omega_H$, the appropriate factor was 2.5. In these two asymptotic cases Appleton-Lassen and Sen-Wyller give essentially the same results. Between these two cases, as is the case in the polar *D* region here, the best factor to use is graphed by Deeks (1966) and is between 1.5 and 2.5 but the agreement between Appleton-Lassen and Sen-Wyller is then only approximate. Singer et al. (2011), in their appropriate Sen-Wyller equations, model the monoenergetic collision frequency as $\nu_m = Kp$, where p is the pressure at height, h, and $K = 6.4 \times 10^5$, all in SI units (Friedrich & Torkar, 1983). From the MSIS-E-90 atmospheric model (https://omniweb.gsfc.nasa.gov/vitmo/msis_vitmo.html), at 69°N, at 70 km, in early June 2013, the neutral number density, $n = 2.36 \times 10^{21}$ m^{-3}, the neutral temperature, $T = 224$ K, and so $p = nkT = 2.36 \times 10^{21} \times 1.38 \times 10^{-23} \times 224 = 7.29$ Pa giving $\nu_m = Kp = 4.67$ MHz. From Figure 2 of Deeks (1966), the appropriate factor discussed above is ~2.2 so the appropriate collision frequency, ν, for use in (Appleton-Lassen) LWPC is $\nu \approx 4.67 \times 2.2 \approx 10.3$ MHz at 70 km. (This 10.3 MHz is about twice LWPC's default built-in collision frequency.)

The finding here of $H' = 73.7$ km and $\beta = 0.32$ km^{-1} for the DHO-Nome path means that $\omega_r = 2.5 \times 10^5$ rad/s at 73.7 km; so at 70 km $\omega_r = 2.5 \times 10^5 \exp[(70–73.7) \times 0.32] = 7.65 \times 10^4 = 3183 N_e/\nu$ (from above), which, using $\nu = 10.3$ MHz from above, results in $N_e \approx 2.5 \times 10^8$ m^{-3} or 250 cm^{-3} at 70 km, in agreement with the values of 200–300 cm^{-3} found at 70 km at 69°N by Singer et al. (2011) using their MF radar and rocket profiles. This also provides further support that the 90° ambiguity was correctly resolved earlier in Figure 3, as $H' = 73.7$ km with $\beta = 0.32$ km^{-1} because $H' = 70.7$ km with $\beta = 0.30$ km^{-1} would have given the electron density at 70 km as ~650 cm^{-3}, while $H' = 77.0$ km with $\beta = 0.335$ km^{-1} would have given the electron density at 70 km as ~80 cm^{-3}, which are both very different from the Singer et al. (2011) values.

5.5. Comparison With Lower Latitudes: EPP Inferred

At a geomagnetic dip latitude of ~52.5°, and a solar zenith angle of ~70° (very similar to that of DHO-Nome path here), Thomson et al. (2017), using the short DHO-Eskdalemuir path, found $H' = 76$ km with $\beta = 0.28$ km^{-1} which corresponds to electron number densities, N_e ~150 and ~250 cm^{-3} at heights of 70 and 74 km, respectively (using the collision frequency of Singer et al. (2011) as in section 5.4 here) while the polar values $H' = 73.7$ km with $\beta = 0.32$ km^{-1} found here give N_e ~250 and ~500 cm^{-3} (larger by a factor of ~1.8) at these same heights. Lin et al. (1963) using a Geiger tube in the Explorer 7 satellite found that, due to reducing geomagnetic shielding, the galactic cosmic ray intensity increases quite rapidly with increasing latitude and L value until the "knee" L value is reached at L ~2.6; the intensity then rises only slightly more reaching a plateau of constant level extending from L ~2.9 toward the poles. The DHO-Eskdalemuir path spans about 2° in latitude with a midpoint at 54.3°N, 2.4°E (geographic) which corresponds to a (CGM) L value of ~2.55. From Figure 3 of Lin et al. (1963), it can be estimated that the galactic cosmic ray intensity at the plateau (i.e., in polar regions) is only <~5% above that for the DHO-Eskalemuir path. Assuming no significant change in recombination rates between ~54°N and the Arctic, this means that there must be another significant nonsolar ionizing source in the polar regions; this is likely to be energetic particle precipitation (EPP),

consistent with the VLF and satellite study of Neal et al. (2015). Satisfactory modeling of the high-latitude *D* region, to match quiet day VLF diurnal amplitude variations, has also been found to require a low background level of EPP "drizzle" (Clilverd et al., 2006; Rodger et al., 2010), such as with electron energies >~300 keV (e.g., Artamonov et al., 2016; Kirkwood & Osepian, 1995). If the recombination rate is approximately proportional to the product of the electron and ion densities, that is, to N_e^2, as is commonly assumed (e.g., Osepian et al., 2009), then N_e being greater by a factor of ~1.8, as above, would mean that polar production is greater by a factor of ~3, which would make this additional ionization (EPP) dominant in the polar *D* region, but only just.

Vampola and Gorney (1983) used the electron spectrometer on the S3–2 satellite to measure precipitating electrons in the range 36–317 keV and found (their Figures 9 and 10) that, at heights ~70 km, the average (quiet and disturbed) precipitating electrons produced ionization ~10 times greater than high-latitude galactic cosmic rays. These average precipitating electron fluxes did not seem to increase very strongly with *L* value in their range *L* = 2–13 (their Figures 2, 6, 7, 9, and 10). Halford et al. (2016) observed quiet time electron precipitation fluxes which were also largely independent of *L* over the Antarctic polar region. They reported precipitating electron bremsstrahlung energy spectra up to several hundred keV from six BARREL high-altitude (~30 km) balloons above the Antarctic "covering *L* values from the inner magnetosphere out to regions of open field lines" on 7 January 2014 during, and preceded by, a long quiet period (followed by an active period after ~16 UT). Their spectra are color coded with the (readily identifiable) yellow/green transition corresponding to 1 count/keV/s. In the quiet time before 16 UT, this count rate occurs for energies, averaging ~230 keV, in the rather small range of 215–240 keV for all six balloons over their wide range of *L* values. This implies that the count rate for their >~300-keV energies is also similarly constant over their wide range of *L* values.

6. Summary and Conclusions

Although the number of VLF transmitters at middle to high latitudes is small, and many of these transmitters have low (and so significantly uncertain) conducting ground north of them, two suitable nearly all-sea long paths across the Arctic passing near the North Pole were able to be found. Along these two paths, DHO-Nome and JXN-Nome, there was no thick ice and the relatively little land was readily allowed for (using LWPC and its built-in ground-conductivity map). Phase (GPS-referenced) and amplitude were measured both near the two transmitters and at Nome allowing a comparison with calculated phases and amplitudes from the U.S. Navy code LWPC for a suitable range of *D* region parameters, H' and β. From the DHO-Nome path the daytime polar *D* region was found to be characterized by height and sharpness $H' = 73.7 \pm 0.7$ km and $\beta = 0.32 \pm 0.02$ km^{-1}, in summer at least at the weak solar maximum in 2013. Reasonable agreement was found with similar results from the JXN-Nome path, despite some degradation due to amplitude uncertainties relating to the radiated power of JXN. These Arctic polar *D* region values should also be valid for the polar Antarctic *D* region. These polar values can be contrasted with summer midday values at low latitude, $H' = 69.3 \pm 0.3$ km, $\beta = 0.49 \pm 0.02$ km^{-1} (Thomson et al., 2014), and at (high) midlatitude, $H' = 72.8 \pm 0.2$ km, $\beta = 0.345 \pm 0.015$ km^{-1} (Thomson et al., 2017).

From VLF recordings on two subarctic VLF paths, between Iceland and the UK (55°–64°N), the variations during daylight of phase, amplitude, H', and β were found to be much less than on lower latitude paths indicating that, unlike at lower latitudes, solar Lyman α (with higher but still varying solar zenith angles) was no longer the dominant ionizing source in the lower *D* region but that energetic particle precipitation (>~300 keV for electrons), assisted by galactic cosmic rays, has the dominant ionizing role at high latitudes. This insensitivity to solar zenith angle at high latitudes also meant that, for the DHO-Nome and JXN-Nome paths, any small changes in solar zenith angle (from typically ~70°, i.e., the Sun ~20° above the horizon) along the path, and during the measurement periods, did not need to be corrected for.

Good agreement was found between *D* region electron densities at 70 km derived by Singer et al. (2011) from MF radar and rockets at 69°N in Norway and those derived from the VLF parameters measured here when the same electron-neutral collision frequencies were used for both.

Acknowledgments
The phase meter used with the portable loop measurements was skillfully designed and constructed by David Hardisty at the University of Otago. The recorded data used in Figures 2, 4, and 5 can be found at http://psddb.nerc-bas.ac.uk. The raw data measurements underlying the observations in Figures 3 and 6 are available in the supporting information. The solar zenith angles came from https://www.esrl.noaa.gov/gmd/grad/solcalc/, *L* values from https://omniweb.gsfc.nasa.gov/vitmo/cgm_vitmo.html, and MSIS-E-90 atmospheric data from https://omniweb.gsfc.nasa.gov/vitmo/msis_vitmo.html. Sunspot numbers and $F_{10.7}$ solar fluxes came from http://www.swpc.noaa.gov/products/solar-cycle-progression and ftp://ftp.swpc.noaa.gov/pub/weekly/RecentIndices.txt.

References

Aggarwal, K. M., Nath, N., & Setty, C. S. G. K. (1979). Collision frequency and transport properties of electrons in the ionosphere. *Planetary and Space Science*, *27*(6), 753–768. https://doi.org/10.1016/0032-0633(79)90004-7

Artamonov, A. A., Mishev, A. L., & Usoskin, I. G. (2016). Atmospheric ionization induced by precipitating electrons: Comparison of CRAC:EPII model with a parameterization model. *Journal of Atmospheric and Solar-Terrestrial Physics*, *149*, 161–166. https://doi.org/10.1016/j.jastp.2016.04.020

Banks, P. M., & Kockarts, G. (1973). *Aeronomy*. New York, NY: Academic.

Brasseur, G. P., & Solomon, S. (2005). *Aeronomy of the Middle Atmosphere*. Dordrecht: Springer.

Budden, K. G. (1965). Effect of electron collisions on the formulas of magneto-ionic theory. *Radio Science Journal of Research NBS/USNC-URSI*, *69D*, 191–211. https://nvlpubs.nist.gov/nistpubs/jres/69D/jresv69Dn2p191_A1b.pdf

Budden, K. G. (1988). *The Propagation of Radio Waves: The Theory of Radio Waves of Low Power in the Ionosphere and Magnetosphere*. Cambridge: Cambridge University Press.

Clilverd, M. A., Rodger, C. J., Thomson, N. R., Brundell, J. B., Ulich, T., Lichtenberger, J., Cobbett, N., et al. (2009). Remote sensing space weather events: The AARDDVARK network. *Space Weather*, *7*, S04001. https://doi.org/10.1029/2008SW000412

Clilverd, M. A., Seppälä, A., Rodger, C. J., Thomson, N. R., Verronen, P. T., Turunen, E., Ulich, T., et al. (2006). Modeling polar ionospheric effects during the October–November 2003 solar proton events. *Radio Science*, *41*, RS2001. https://doi.org/10.1029/2005RS003290

Comité Consultatif International des Radiocommunications (1990). Radio propagation and circuit performance at frequencies below about 30 kHz. (Report 895–2, 29 pp., Dusseldorf, Germany). https://www.itu.int/dms_pub/itu-r/opb/rep/R-REP-P.895-2-1990-PDF-E.pdf

Danilov, A. D., Smirnova, N. V., Blix, T. A., Thrane, E. V., & Vanina, L. B. (2003). Some features of electron density behaviour in the high latitude D-region derived from in situ measurements. *Journal of Atmospheric and Solar-Terrestrial Physics*, *65*(4), 417–427. https://doi.org/10.1016/S1364-6826(02)00198-0

Deeks, D. G. (1966). Generalised full wave theory for energy-dependent collision frequencies. *Journal of Atmospheric and Terrestrial Physics*, *28*(9), 839–846. https://doi.org/10.1016/S0021-9169(17)30005-3

Ferguson, J. A. (1980). *Ionospheric Profiles for Predicting Nighttime VLF/LF Propagation (Nav. Ocean Syst. Cent. Technical Report 530)*. Springfield, VA: National Technical Information Service. http://www.dtic.mil/dtic/tr/fulltext/u2/a085399.pdf

Ferguson, J. A., & Snyder, F. P. (1990). *Computer Programs for Assessment of Long Wavelength Radio Communications, Version 1.0: Full FORTRAN Code User's Guide. (Naval Ocean Systems Center Tech. Doc. 1773, DTIC AD-B144 839)*. Alexandria, VA: Defense Technical Information Center.

Forbush, S. E. (1958). Cosmic-ray intensity variations during two solar cycles. *Journal of Geophysical Research*, *63*(4), 651–669. https://doi.org/10.1029/JZ063i004p00651

Friedrich, M., Finsterbusch, R., Torkar, K. M., & Spöcker, H. (1991). A further generalisation of the Sen and Wyller magneto-ionic theory. *Advances in Space Research*, *11*(10), 105–108. https://doi.org/10.1016/0273-1177(91)90330-M

Friedrich, M., & Torkar, K. M. (1983). Collision frequencies in the high latitude *D*-region. *Journal of Atmospheric and Terrestrial Physics*, *45*(4), 267–271. https://doi.org/10.1016/S0021-9169(83)80048-8

Friedrich, M., & Torkar, K. M. (2001). FIRI: A semiempirical model of the lower ionosphere. *Journal of Geophysical Research*, *106*(A10), 21,409–21,418. https://doi.org/10.1029/2001JA900070

Halford, A. J., McGregor, S. L., Hudson, M. K., Millan, R. M., & Kress, B. T. (2016). BARREL observations of a solar energetic electron and solar energetic proton event. *Journal of Geophysics Research: Space Physics*, *121*, 4205–4216. https://doi.org/10.1002/2016JA022462

International Telecommunications Union (1999). World atlas of ground conductivities (Recommendation ITU-R P.832–2, 49 pp.) https://www.itu.int/dms_pubrec/itu-r/rec/p/R-REC-P.832-2-199907-S!!PDF-E.pdf

Kirkwood, S., & Osepian, A. (1995). Quantitative studies of energetic particle precipitation using incoherent scatter radar. *Journal of Geomagnetism and Geoelectricity*, *47*(8), 783–799. https://doi.org/10.5636/jgg.47.783

Kwok, R., & Rothrock, D. A. (2009). Decline in Arctic Sea ice thickness from submarine and ICESat records: 1958–2008. *Geophysical Research Letters*, *36*, L15501. https://doi.org/10.1029/2009GL039035

Lin, W. C., Venkatesan, D., & Van Allen, J. A. (1963). Latitude survey of cosmic-ray intensity by Explorer 7, October 1959 to February 1961. *Journal of Geophysical Research*, *68*(17), 4885–4896. https://doi.org/10.1029/JZ068i017p04885

McNeill, D., & Hoekstra, P. (1973). In-situ measurements on the conductivity and surface impedance of sea ice at VLF. *Radio Science*, *8*(1), 23–30. https://doi.org/10.1029/RS008i001p00023

Morfitt, D. G. (1977). *Effective Electron Density Distributions Describing VLF/ELF Propagation Data (Nav. Ocean Syst. Cent. Tech. Rep. 141)*. Springfield, VA: National Technical Information Service. http://www.dtic.mil/dtic/tr/fulltext/u2/a047508.pdf

Morfitt, D. G., & Shellman, C. H. (1976). *"MODESRCH", an Improved Computer Program For Obtaining ELF/VLF/LF Mode Constants in an Earth-Ionosphere Waveguide (Naval Electr. Lab. Cent. Interim Rep. 77T, NTIS Accession ADA032573)*. Springfield, VA: National Technical Information Service. http://www.dtic.mil/dtic/tr/fulltext/u2/a032573.pdf

Morgan, R. R. (1968). *World-Wide VLF Effective-Conductivity Map (Westinghouse Rep. 80133F-1)*. Springfield, VA: National Technical Information Service. http://www.dtic.mil/dtic/tr/fulltext/u2/675771.pdf

Neal, J. J., Rodger, C. J., Clilverd, M. A., Thomson, N. R., Raita, T., & Ulich, T. (2015). Long-term determination of energetic electron precipitation into the atmosphere from AARDDVARK subionospheric VLF observations. *Journal of Geophysical Research: Space Physics*, *120*, 2194–2211. https://doi.org/10.1002/2014JA020689

Neher, H. V., & Anderson, H. R. (1962). Cosmic rays at balloon altitudes and the solar cycle. *Journal of Geophysical Research*, *67*(4), 1309–1315. https://doi.org/10.1029/JZ067i004p01309

Osepian, A., Kirkwood, S., Dalin, P., & Tereschenko, V. (2009). *D*-region electron density and effective recombination coefficients during twilight—Experimental data and modelling during solar proton events. *Annales Geophysicae*, *27*(10), 3713–3724. https://doi.org/10.5194/angeo-27-3713-2009

Pack, J. L., & Phelps, A. V. (1961). Drift velocities of slow electrons in helium, neon, argon, hydrogen, and nitrogen. *Physical Review*, *121*(3), 798–806. https://doi.org/10.1103/PhysRev.121.798

Perovich, D., Meier, W., Tschudi, M., Farrell, S., Hendricks, S., Gerland, S., et al. (2017). Sea ice, Arctic essays, http://www.arctic.noaa.gov/Report-Card/Report-Card-2017/ArtMID/7798/ArticleID/699/Sea-Ice

Phelps, A. V., & Pack, J. L. (1959). Electron collision frequencies in nitrogen and in the lower ionosphere. *Physical Review Letters*, *3*(7), 340–342. https://doi.org/10.1103/PhysRevLett.3.340

Rodger, C. J., Clilverd, M. A., Seppälä, A., Thomson, N. R., Gamble, R. J., Parrot, M., Sauvaud, J.-A., et al. (2010). Radiation belt electron precipitation due to geomagnetic storms: Significance to middle atmosphere ozone chemistry. *Journal of Geophysical Research*, *115*, A11320. https://doi.org/10.1029/2010JA015599

Sen, H. K., & Wyller, A. A. (1960a). Generalization of the Appleton-Hartree magneto-ionic formula. *Physical Review Letters*, *4*(7), 355–357. https://doi.org/10.1103/PhysRevLett.4.355

Sen, H. K., & Wyller, A. A. (1960b). On the generalization of the Appleton-Hartree magnetoionic formulas. *Journal of Geophysical Research*, *65*(12), 3931–3950. https://doi.org/10.1029/JZ065i012p03931

Singer, W., Latteck, R., Friedrich, M., Wakabayashi, M., & Rapp, M. (2011). Seasonal and solar activity variability of *D*-region electron density at 69°N. *Journal of Atmospheric and Solar-Terrestrial Physics*, *73*(9), 925–935. https://doi.org/10.1016/j.jastp.2010.09.012

Størmer, C. (1955). *The Polar Aurora*. Oxford: Clarendon Press.

Thomson, N. R., Clilverd, M. A., & Rodger, C. J. (2014). Low-latitude ionospheric *D* region dependence on solar zenith angle. *Journal of Geophysical Research: Space Physics*, *119*, 6865–6875. https://doi.org/10.1002/2014JA020299

Thomson, N. R., Clilverd, M. A., & Rodger, C. J. (2017). Midlatitude ionospheric *D* region: Height, sharpness, and solar zenith angle. *Journal of Geophysical Research: Space Physics*, *122*, 8933–8946. https://doi.org/10.1002/2017JA024455

Tschudi, M. A., Stroeve, J. C., & Stewart, J. S. (2016). Relating the age of arctic sea ice to its thickness, as measured during NASA's ICESat and IceBridge campaigns. *Remote Sensing*, *8*(6), 457–469. https://doi.org/10.3390/rs8060457

Vampola, A. L., & Gorney, D. J. (1983). Electron energy deposition in the middle atmosphere. *Journal of Geophysical Research*, *88*(A8), 6267–6274. https://doi.org/10.1029/JA088iA08p06267

Vincenty, T. (1975). Direct and inverse solutions of geodesics on the ellipsoid with application of nested equations. *Survey Review*, *23*(176), 88–93. https://doi.org/10.1179/sre.1975.23.176.88

Wait, J. R., & Spies, K. P. (1964). *Characteristics of the Earth-Ionosphere Waveguide for VLF Radio Waves. (NBS Tech. Note 300)*. Boulder, CO: National Bureau of Standards. https://nvlpubs.nist.gov/nistpubs/Legacy/TN/nbstechnicalnote300.pdf

Watt, A. D. (1967). *VLF Radio Engineering*. Oxford: Pergamon Press.